Materials Today Bio 24 (2024) 100885

Contents lists available at ScienceDirect

Materials Today Bio

journal homepage: www.journals.elsevier.com/materials-today-bio

In vitro and *in vivo* studies on biodegradable Zn porous scaffolds with a drug-loaded coating for the treatment of infected bone defect

Xiang Jin [a,b,1], Dongxu Xie [c,d,1], Zhenbao Zhang [b,1], Aobo Liu [c,d], Menglin Wang [b], Jiabao Dai [c,d], Xuan Wang [a,b], Huanze Deng [b], Yijie Liang [a,b], Yantao Zhao [b,e,f,***], Peng Wen [c,d,**], Yanfeng Li [b,a,*]

[a] Postgraduate Training Base, Jinzhou Medical University and The Fourth Medical Centre, Chinese PLA General Hospital, Beijing, 10048, China
[b] Department of Stomatology, The Fourth Medical Centre, PLA General Hospital, Beijing, 100048, China
[c] State Key Laboratory of Tribology in Advanced Equipment, Beijing, 100084, China
[d] Department of Mechanical Engineering, Tsinghua University, Beijing, 100084, China
[e] Senior Department of Orthopedics, The Fourth Medical Centre, PLA General Hospital, Beijing, 100048, China
[f] Beijing Engineering Research Center of Orthopedics Implants, Beijing, 100048, China

ARTICLE INFO

Keywords:
Additive manufacturing
Pure Zn
Porous scaffold
Bone repair
Anti-infection

ABSTRACT

Additively manufactured biodegradable zinc (Zn) scaffolds have great potential to repair infected bone defects due to their osteogenic and antibacterial properties. However, the enhancement of antibacterial properties depends on a high concentration of dissolved Zn^{2+}, which in return deteriorates osteogenic activity. In this study, a vancomycin (Van)-loaded polydopamine (PDA) coating was prepared on pure Zn porous scaffolds to solve the above dilemma. Compared with pure Zn scaffolds according to comprehensive *in vitro* tests, the PDA coating resulted in a slow degradation and inhibited the excessive release of Zn^{2+} at the early stage, thus improving cytocompatibility and osteogenic activity. Meanwhile, the addition of Van drug substantially suppressed the attachment and proliferation of *S. aureus* and *E. coli* bacterial. Furthermore, *in vivo* implantation confirmed the simultaneously improved osteogenic and antibacterial functions by using the pure Zn scaffolds with Van-loaded PDA coating. Therefore, it is promising to employ biodegradable Zn porous scaffolds with the proposed drug-loaded coating for the treatment of infected bone defects.

1. Introduction

Bone defects resulting from trauma, tumors, surgical resection, and other factors are relatively prevalent, often presenting as pain and dysfunction at the defect site, which seriously affects the quality of life of patients [1–3]. Bone repair treatment is necessary when a bone defect fails to heal spontaneously. Although autologous bone transplantation is the "gold standard" for bone repair, it is being substituted with bone repair implants due to drawbacks such as donor area injury and effects on donor area function [4]. The implantation of implants may lead to local foreign body reactions and reduce local immune resistibility, which facilitates bacterial colonization and infection [5–7]. As a result, despite strict aseptic procedures during the implant procedure, infections in the surgical area can still occur, and in very severe cases infections can be fatal [8]. The high risk of infection persists for a minimum of 6 months after the implant is removed [9]. Biodegradable antibacterial implants present a promising approach to address the underlying infection problem. Such an implant can offer mechanical support during the initial stages of bone repair, and gradually degrade and disappear, which eliminates the conductive platform for bacterial survival, and sustains anti-infection during the repair process.

As a biodegradable metal, pure zinc (Zn) scaffolds are gradually considered as potential bone implants. Compared with other biodegradable bone repair materials, such as polymers, pure Zn presents superior mechanical properties [10]. Moreover, a relatively suitable degradation rate is observed in pure Zn compared with biodegradable

* Corresponding author. Department of Stomatology, The Fourth Medical Centre, PLA General Hospital, Beijing, 100048, China.
** Corresponding author. State Key Laboratory of Tribology in Advanced Equipment, Beijing, 100084, China.
*** Corresponding author. Department of Stomatology, the Fourth Medical Centre, PLA General Hospital, Beijing, 100048, China.
E-mail addresses: userzyt@qq.com (Y. Zhao), wenpeng@tsinghua.edu.cn (P. Wen), 949427779@qq.com (Y. Li).
[1] Xiang Jin, Dongxu Xie and Zhenbao Zhang contributed equally to the manuscript and should be considered co-first authors.

https://doi.org/10.1016/j.mtbio.2023.100885
Received 19 September 2023; Received in revised form 17 November 2023; Accepted 27 November 2023
Available online 1 December 2023

magnesium (Mg) and ferrum (Fe) [11,12]. The Zn^{2+} released during the degradation of pure Zn modulates the biological behavior of cells in a concentration-dependent manner [13,14]. For example, low concentrations of Zn^{2+} lead to good cytocompatibility, promoting the function of osteoblasts, whereas excessive concentrations of Zn^{2+} are cytotoxic [15,16]. Furthermore, pure Zn also exhibits excellent antibacterial properties [5,17,18]. During the degradation of scaffolds, Zn^{2+} induces the generation of reactive oxygen species (ROS), causing bacterial death by damaging the cell membranes of bacteria [8]. Because of these properties, pure Zn shows a potential for application as antibacterial orthopedic implant. However, high concentrations of Zn^{2+} release are beneficial to antibacterial function for Zn implants, which is the inverse of the low concentration of Zn^{2+} required for osteogenesis [16,17]. Moreover, bone is an extremely intricate human organ in terms of morphology and structure. This complexity poses challenges for the manufacture of Zn implants in matching the individual needs of bone defect repair [19].

Additive manufacturing (AM) technology provides a way to produce bone implants with intricate geometries and customized structures. It enables the modulation of mechanical properties and degradation behavior of Zn implants through the customization of porous structures [20,21]. The porous structures are designed to better match the elastic modulus of cancellous bone, avoiding the stress-shielding effect. The porous structures can promote the inward growth of osteoblasts and blood vessels, as well as enable the transport of metabolic waste and nutrients [22–26]. In addition, studies have reported that laser powder bed fusion (L-PBF) technology enhanced the mechanical properties of pure Zn by grain refinement [20,27]. Furthermore, the increased surface area and permeability of Zn porous scaffolds fabricated by L-PBF significantly accelerated degradation [28]. The accelerated degradation rate led to a higher release of Zn^{2+}, which enhanced the antibacterial property of the Zn implants but also inhibited bone repair. Xia et al. [11] reported that significant bone regeneration was observed in the internal pores of the L-PBF pure Zn scaffolds after 12 weeks of implantation. However, osseointegration was delayed in the early stages of bone repair due to excessive Zn^{2+} release. Many strategies have been developed to improve the antibacterial and osteogenic activity of Zn scaffolds. For instance, Zn–Cu and Zn–Ag alloys have been designed to inhibit bacterial growth through the co-release of Zn^{2+} and Cu^{2+}/Ag^{+} [9,29–31]. Additionally, Zn–Cu and Zn–Ag alloys can also promote osteogenic differentiation and inhibit osteolytic properties [9,30,31]. However, the potential toxicity of Cu^{2+}, Ag^{+}, and high concentrations of Zn^{2+} remains a significant concern [32]. As a result, it is crucial to explore additional approaches to enhance the antibacterial property of pure Zn safely and effectively, while ensuring the controlled release of low concentrations of Zn^{2+} that promote bone repair.

Surface modification can provide a functionalized surface for bone implants to modulate degradation and improve biological function [33–35]. Su et al. [36] utilized Zn phosphate coating to decelerate the degradation rate of pure Zn to improve biocompatibility. Chitosan coating on the surface of Zn-0.8Li alloy improved cytocompatibility by inhibiting corrosion [37]. Mo et al. [38] fabricated an alendronate-embedded zinc phosphate (ZnP) coating to promote osteoclast apoptosis on the surface of pure Zn using alternating deposition method, which greatly improved the osteogenic ability of pure Zn. Furthermore, by immobilizing antibacterial drugs within the coating, surface modification can greatly improve the antibacterial properties of the substrate. Such antibacterial coatings have been applied to various bulk samples, including stainless steel, Ti alloys, and Mg alloys [39–42]. However, many surface coating procedures concentrate on uniformly coating the outside surface of bulk materials, while ignoring how to generate a uniform and dense coating on the outer and inner surfaces of porous scaffolds [39–43].

Polydopamine (PDA), a synthetic polymer inspired by mussel adhesion proteins, is capable of forming functionalized coatings with adhesion properties on almost any material surface via Michael addition or Schiff base reaction in a weak alkaline condition and is unaffected by the shape and structures of substrate [44–46]. Furthermore, PDA exhibits antibacterial properties and has been extensively studied as a freestanding or composite antibacterial materials. Meanwhile, its abundant active functional groups, such as catechol groups and primary amine groups, can serve as secondary reaction platforms for binding with antibiotics or growth factors for secondary modification of the substrate material to improve antibacterial and osteogenic functions [47–49]. The application of antibiotic-loaded PDA coating on Zn porous scaffolds may provide a safe and effective strategy to improve both the antibacterial and osteogenic properties of the scaffolds at the same time. In our previous work [50], a hydroxyapatite (HA)/PDA composite coating has been constructed on the Zn–1Mg porous scaffolds with PDA as an intermediate interfacial layer. Meanwhile, antibacterial drugs and bioactive growth factors were loaded in the composite coating to improve the antibacterial and osteogenic functions of the Zn–1Mg scaffolds. Interestingly, the PDA coating loaded only with antibacterial drugs also exhibited an improved osteointegration and osteoinduction *in vivo*. Though composite coating offers great possibilities for simultaneously improving the antibacterial and osteogenic properties, the preparation process of PDA coating on the Zn scaffolds and their impact on the performance of the scaffolds have not been thoroughly discussed.

In the present study, pure Zn porous scaffolds were fabricated by L-PBF, and the vancomycin (Van)-loaded PDA coating was constructed on the outer and inner surfaces of the scaffolds. The coated scaffolds' degradation behavior, biocompatibility, and osteogenic and antibacterial properties were comprehensively investigated. The degradation rate of the pure Zn porous scaffolds was delayed by the physical blocking effect of the PDA coating. The changed surface physicochemical properties induced by the PDA coating and the low concentration of released Zn^{2+} improved the biocompatibility and osteogenic activity of the pure Zn scaffolds together. Furthermore, the Van loaded on the coating greatly enhanced the antibacterial property, thus making pure Zn scaffolds more promising for antibacterial bone implants.

2. Materials and methods

2.1. Samples preparation

2.1.1. Preparation of AM pure Zn porous scaffolds

Pure Zn rods were cast and atomized with nitrogen to produce powder (Nanoval, Germany) with an average particle size of 19.57 μm (D_{50}). A scanning electron microscope (SEM, Zeiss, Germany) equipped with an energy dispersive spectrometer (EDS, Ametek, USA) was used to observe the powder shape, and the majority of the pure Zn powder was spherical (Fig. S1a). A 25 mm thick pure Zn sheet metal was used as the substrate. Before processing, the powders were dried at 70 °C for 4 h to remove humidity. A laboratory L-PBF machine (BLT S210, China) was used for pure Zn sample fabrication (Figs. S1b and c). The geometry of porous samples for *in vitro* tests was pre-defined as φ10 mm × 2.55 mm with a pore size of 600 μm and a strut thickness of 450 μm. The samples for *in vivo* tests were determined as a cylinder with a dimension of φ2.55 mm × 5.7 mm, and having the same pore parameters as *in vitro* ones. A 1070 nm ytterbium fiber laser (IPG Photonics, USA) with a focus diameter of 75 μm was employed. The procedure was carried out in an argon-shielded chamber with a residual oxygen level of less than 100 ppm. To mitigate the adverse effects of evaporation on process stability, a unique gas circulation system was developed. Based on the preliminary results for the optimization of dimensional accuracy of scaffolds, the laser energy input for all samples was set to laser power = 30 W, scanning speed = 700 mm/s, hatching space = 50 μm, and layer thickness = 30 μm. The Zn porous scaffolds fabricated by L-PBF were named as pure Zn.

2.1.2. Preparation of Van-loaded PDA coating

Pure Zn samples were ultrasonically cleaned and polished with

acetone, ethanol absolute, chemical polishing solution (concentrated sulfuric acid 3 mL/L, 30 % H_2O_2 70 mL/L), and ultrapure water, respectively. The dried samples were deposited in a hydrothermal reactor with a 1 mol/L NaOH solution and placed in a 120 °C oven for 4 h. After removing and cleaning the samples, they were placed in a 120 °C oven for 1 h. The obtained samples were labeled as activated Zn.

The PDA and PDA@Van coating deposition solutions were made with an ethanol absolute/ultrapure water (3: 7) combination containing 1 mg/mL dopamine (DA, Aladdin, China), 1 mg/mL Van hydrochloride (Aladdin, China), and 20 mM 2-piperidine ethanol (Aladdin, China). Activated Zn samples were suspended in the deposition solution and kept at 37 °C for 24 h. Following that, the samples were taken out, turned over, and repeated once to finish the coating, and the samples were labeled as PDA@Van/Zn. The PDA/Zn samples without Van were prepared according to the same procedure.

2.2. Samples characterization

2.2.1. Microstructure, composition and water contact angle

The morphology and element composition of the scaffold surface and cross-section of the scaffolds were examined by SEM and EDS. The chemical composition was determined using an X-ray diffractometer (XRD, Rigaku SmartLab 9 kW, Japan) and attenuated total reflection Fourier transform infrared spectroscopy (ATR-FTIR, Thermo Scientific Nicolet iS20, USA). The water contact angle was measured using a goniometer (JC2000DM, ZYKX, China).

2.2.2. Van release analysis

PDA@Van/Zn samples were infiltrated into 20 mL phosphate buffer solution (PBS, pH = 7.4) and incubated in a shaker at 37 °C and 80 rpm. At specific time points (0.5 h, 1 h, 2 h, 4 h, 16 h, 32 h, 3 d, 6 d, 12 d, and 24 d), 1 mL of PBS was removed for evaluation and displaced by an equal quantity of fresh PBS. The Van concentration was measured at 236 nm using an ultraviolet–visible spectrophotometer (Ultrospec 1100pro, USA).

2.2.3. In vitro degradation behavior

The electrochemical workstation (Autolab, Metrohm, Switzerland) with a three-electrode system (saturated calomel used as reference electrode, platinum used as counter electrode, and samples used as working electrode) was utilized. The samples of each group were immersed in modified simulated body fluid (*m*-SBF, Table S1) for 3600 s to stabilize the open circuit potential before the test. PDP scan was performed at a scan rate of 1 mV/s with a potential range of −1.6 V to −0.4 V. The Tafel linear extrapolation method was used to calculate the corrosion potential (E_{corr}) and corrosion current density (i_{corr}). EIS measurements were performed over a frequency range of 10^{-2}–10^{-5} Hz with a perturbation of 10 mV. The equivalent circuits were obtained by ZSimpWin software.

The immersion tests were conducted in *m*-SBF solution at 37 °C. The *m*-SBF was refreshed every 2 days for 28 days. After removing the samples, carefully rinse them with ultrapure water. The weight change of the samples was recorded. The morphology of the corroded scaffold surface was observed by SEM. The concentration of Zn^{2+} in the *m*-SBF solution was measured by inductively coupled plasma-mass spectrometry (ICP-MS, Agilent 7700, USA).

2.3. In vitro cellular and bacterial tests

2.3.1. Cell viability and morphological analysis

All samples were sterilized by cobalt 60 irradiation. In this study, Mouse embryo osteoblast precursor cells (MC3T3-E1) were from the Cell Bank of the Chinese Academy of Sciences (Shanghai, China), and cultured with α-MEM (Gibco, USA) complete medium containing 10 % fetal bovine serum (FBS, Gibco, USA) and 1 % penicillin-streptomycin solution (Solarbio, China) at 37 °C, 5 % CO_2. The preparation of the sample extracts followed ISO 10993–5. The scaffolds were immersed in the complete culture medium with an extraction ratio of 1.25 cm^2/mL at 37 °C for 24 ± 0.5 h in a cell incubator. Recent research [8,51] demonstrated that Zn alloy exhibited a slow degradation rate *in vivo*, while the metabolism of corrosion products occurred rapidly. Therefore, extract concentrations of 30 % and 10 % were selected for the *in vitro* cell experiments. The cell viability was detected using a cell counting kit-8 (CCK-8, APExBIO, USA). MC3T3-E1 cells were inoculated in 96-well plates at a cell concentration of 2×10^3/well. After the cell adhesion, the initial medium was displaced with the sample extracts, while α-MEM complete medium was used as the negative control group. At cultured 1, 3, and 5 days, the original culture medium was replaced with 100 μL serum-free medium including 10 μL CCK-8 solution. The cells were incubated in darkness at 37 °C for 30 min. The optical density (OD) of each well was detected at 450 nm using an enzyme-labeling instrument (Thermo Fisher, USA). As for Live/dead cells stain, the cells were inoculated in 12-well plates, and cultured with sample extracts for 1 day. A Live/dead cell staining kit (Beyotime, China) was used to evaluate the survival state of cells. The cells' morphology and distribution on the scaffolds' surfaces were analyzed by SEM. The sterilized samples were co-cultured with MC3T3-E1 cells for 24 h. The samples were washed with PBS, fixed with 4 % paraformaldehyde fix solution, and gradually dehydrated using a gradient of ethanol at concentrations of 30 %, 50 %, 70 %, 80 %, 90 %, 95 %, 100 %, and 100 %. The adhesion status and the number of cells on the scaffolds were observed.

2.3.2. In vitro osteogenic differentiation

MC3T3-E1 cells were inoculated in 12-well plates at a 1×10^4/mL cell concentration. After the cell adhesion, the initial medium was replaced with the sample extracts containing an osteogenic induction solution (10 mmol/L β-sodium glycerophosphate, 0.05 mmol/L vitamin C and 100 mmol/L dexamethasone). When cultured for 7 and 14 days, the cells were stained using the alkaline phosphatase (ALP) staining kit (Beyotime, China) for qualitative imaging. Pictures of each well were captured using a microscope. In addition, cells were lysed using RIPA lysis buffer (Beyotime, China), and total proteins were extracted. The concentration of total protein was determined by the BCA Protein Assay Kit (Beyotime, China), and ALP activity was measured for each group with an ALP activity detection kit (Beyotime, China). The relative ALP activity was calculated. At day 21, the cells were stained using 0.2 % Alizarin Red S Staining Solution (Beyotime, China) for qualitative imaging. The mineralized nodules were then lysed with 10 % laurylpyridinum chloride (Solarbio, China), and the OD of each group was detected at 570 nm for semi-quantitative analysis.

The relative expression level of osteogenesis-related genes, Runx-2, OCN, and OPN, of MC3T3-E1 cells was evaluated by real-time polymerase chain reaction (RT-PCR). The cells were inoculated in 6-well plates at a 5×10^4/mL cell concentration. After cell adhesion, they were co-cultured with osteogenic induction sample extracts. At day 7, total cellular RNA was extracted using Trizol (Life, USA), and quantified. RNA was reverse-transcribed into cDNA using an RNA-to-cDNA premix kit (Takara, China). The primer sequences were provided in Table S2. The cDNA was mixed with the primers to quantify the gene expression of the target genes. All gene expression data were normalized to GAPDH (Biotech, China) expression data and expressed as a multiple of the blank control.

2.3.3. In vitro antibacterial activity

Staphylococcus aureus (*S. aureus*, ATCC 25923) and *Escherichia coli* (*E. coli*, ATCC 25922) were used to evaluate the antibacterial properties of the scaffolds. *S. aureus* and *E. coli* were suspended in LB broth (Solarbio, China) and incubated in a 37 °C shaker (200 rpm) for 20 h. Finally, the concentrations of the bacterium solutions were specified and diluted. The sterilized samples were co-cultured with 3 mL of bacterial suspension (1×10^7 CFU/mL) for 24 h at 37 °C incubator. The samples and bacterial suspension were collected respectively. The samples were

washed with PBS, fixed with 4 % paraformaldehyde fix solution, and gradually dehydrated using a gradient of ethanol at concentrations of 30 %, 50 %, 70 %, 80 %, 90 %, 95 %, 100 %, and 100 %. The adhesion status and the number of bacteria adhered on the scaffolds were observed using SEM. In addition, the bacterial suspension was diluted in gradients and spread on a trypticase soy agar (TSA) medium, and the number of plate colonies was determined after 24 h of incubation at 37 °C. The long-lasting antibacterial abilities of the different scaffolds were further evaluated. First, the samples were immersed in PBS solution for different times (3 and 7 d) to release antibacterial substances. Subsequently, the samples were removed and lightly washed with PBS solution. The samples were co-cultured with 3 mL of bacterial suspension (1×10^7 CFU/mL) for 24 h at 37 °C incubator. Finally, the bacterial suspension was diluted in gradients and spread on a TSA medium, and the number of plate colonies was observed after 24 h of incubation at 37 °C.

2.4. In vivo implantation

2.4.1. Surgical process

The experimental animals were male Sprague Dawley rats with weights of 200–250 g in this study. The animal experiments were approved by the Animal Ethics Committee of the Beijing Keyu Animal Breeding Center (KYLL0001089). 24 male rats were anesthetized by intraperitoneal injection with ketamine (10 mg/kg, Dr. Ehrenstorfer GmbH, Germany) and 2 % xylazine (10 mg/kg, Fluorochem, UK). The hair near the knee joint was shaved and disinfected. The femoral condyle was revealed through a longitudinal incision made along the lateral face of the patella. Using a pre-sterilized 3.0 mm drill, a bi-cortical perforating bone defect model was created at the lateral femoral condyle. The scaffolds were implanted into the bone defect (Fig. S2). After rinsing with sterile saline, the muscle and skin were stitched layer by layer. They were euthanized 4, 8, and 12 weeks after surgery to collect the femur, which was then immersed in a 4 % paraformaldehyde fix solution for fixation.

2.4.2. Micro-computed tomography (Micro-CT) analysis

The fixed specimens were scanned using Micro-CT (Zeiss Xradia 520 Versa, Germany, 120 kV, 66.7 μA) and imaged using the 3D image processing software CTvox 3.0 (Bruker, Germany). The region of interest (ROI) was defined as a 0.5 mm diameter area around the implant. The bone volume fraction (BV/TV), trabecular numbers (Tb.N), trabecular thickness (Tb.Th), and trabecular separation (Tb.Sp) were analyzed quantitatively to evaluate the bone repair of rats.

2.4.3. Histological analysis

The collected femoral specimens were dehydrated with ethanol, cleaned with dimethylbenzene, and ultimately embedded in methyl methacrylate. Three to four 200 μm-thick sections were cut along the horizontal axis of the femur, ground and polished to 100 μm-thick, stained with methylene blue-basic magenta, and imaged under a microscope. At 12 weeks after implantation, the organ samples of rats, including heart, liver, spleen, lungs, and kidneys were stained with hematoxylin-eosin (H&E).

2.4.4. In vivo antibacterial activity

After constructing a femoral condyle bi-cortical penetrating bone defect model, 10 μl *S. aureus* suspension was injected into the bone defect at a bacterial concentration of 1×10^7 CFU/mL. The scaffolds were inserted into the bone defect. 1 week after implantation, the rats were euthanized to collect the femur and separate the implants. The bacteria of the implants and femur were separated by ultrasound. The isolated bacteria were inoculated and cultured on TSA medium and counted to evaluate the antibacterial activity *in vivo*. In addition, femoral specimens without implants were decalcified and stained with H&E.

2.5. Statistical analysis

IBM SPSS Statistics 26.0 software was used to process the data, and quantitative statistics were expressed as mean ± standard deviation (SD). The student t-test or one-way analysis of variance (ANOVA) was used to compare groups, and differences were regarded as significant at $^*p < 0.05$, $^{**}p < 0.01$, or $^{***}p < 0.001$.

3. Results

3.1. Samples characterization

The morphology of samples was shown in Fig. 1a. The surface of the pure Zn scaffold was covered by a large quantity of residual Zn powders. The residual powder vanished on the surface of the activated Zn after alkali-heat treatment. Instead, an elongated and longitudinal crystal structure was observed on the surface of activated Zn. Numerous uniform-sized PDA microspheres were observed to adhere to columnar crystals on the scaffold surface in the PDA/Zn and PDA@Van/Zn groups. The morphology of PDA microspheres was consistent with the observations in the investigation [52,53]. The results of the EDS analysis were shown in Fig. 1b. Compared with pure Zn, the content of O element on the activated Zn scaffolds increased to 16.90 %, attributed to the production of large amounts of oxides. Besides, the typical N element in PDA was observed on the surface of the coated scaffolds, and the S and Cl elements only presented in Van were observed on the PDA@Van/Zn. These results indicated the successful preparation of the PDA and PDA@Van coating on the surface of pure Zn. The cross-section of samples was shown in Fig. 1c. After alkali-heat treatment, an approximately 40-μm-thick oxide crystal layer was observed on the surface of scaffolds in the activated Zn group, and a large number of PDA microspheres adhered along the oxide crystals.

The XRD pattern was shown in Fig. 1d. Only the Zn peak was detected in the pure Zn group. ZnO peak was observed on the surface of the activated Zn, indicating as the existence of ZnO. As shown in the FTIR spectra (Fig. 1e), the absorption peak of ZnO appeared at 613 cm^{-1} in activated Zn, PDA/Zn, and PDA@Van/Zn. In PDA/Zn and PDA@Van/Zn, a peak near 3320 cm^{-1} was observed, which corresponded to the stretching vibration of the O–H. In addition, the hydroxyl group of catechol C–O and/or C–N at 1262 cm^{-1}, and the characteristic C═C peak at 1678 cm^{-1} indicated the molecular structure of PDA. Furthermore, PDA@Van/Zn had a characteristic peak at 818 cm^{-1} corresponding to Cl^- and N–H vibrational absorption peaks at 1390 cm^{-1}, 1470 cm^{-1}, and 1587 cm^{-1} corresponding to the amide I and II bands, suggesting the successful loading of Van.

Fig. 1f depicted the results of the water contact angle. After alkali-heat treatment, the water contact angle of the pure Zn considerably decreased from 142.0 ± 0.6° to 10.8 ± 2.0°, indicating a significant improvement in hydrophilicity ($p < 0.01$). Although the water contact angle rose slightly after PDA or PDA@Van coating deposition, measuring as 36.7 ± 0.7° and 35.7 ± 1.2°, respectively, the surface still showed hydrophilicity, which was substantially lower than that of pure Zn ($p < 0.01$). The water contact angle of scaffolds ranked as activated Zn < PDA@Van/Zn and PDA/Zn < pure Zn.

Fig. 1g depicted the Van release curve of PDA@Van/Zn. Initially, Van was rapidly released from the scaffolds in the first 40 h, followed by a slow release and finally reaching a gradual plateau. Significantly, after 6 days of a stable release, there was an abrupt increase in the release rate of Van, which could be attributed to the disintegration of the PDA coating.

3.2. In vitro degradation behavior

The electrochemical tests were performed to evaluate the degradation rate. According to Table S3 and Fig. 2a, the E_{corr} value of the pure Zn was approximately −1.350 V_{SCE}. After coating treatment, the E_{corr}

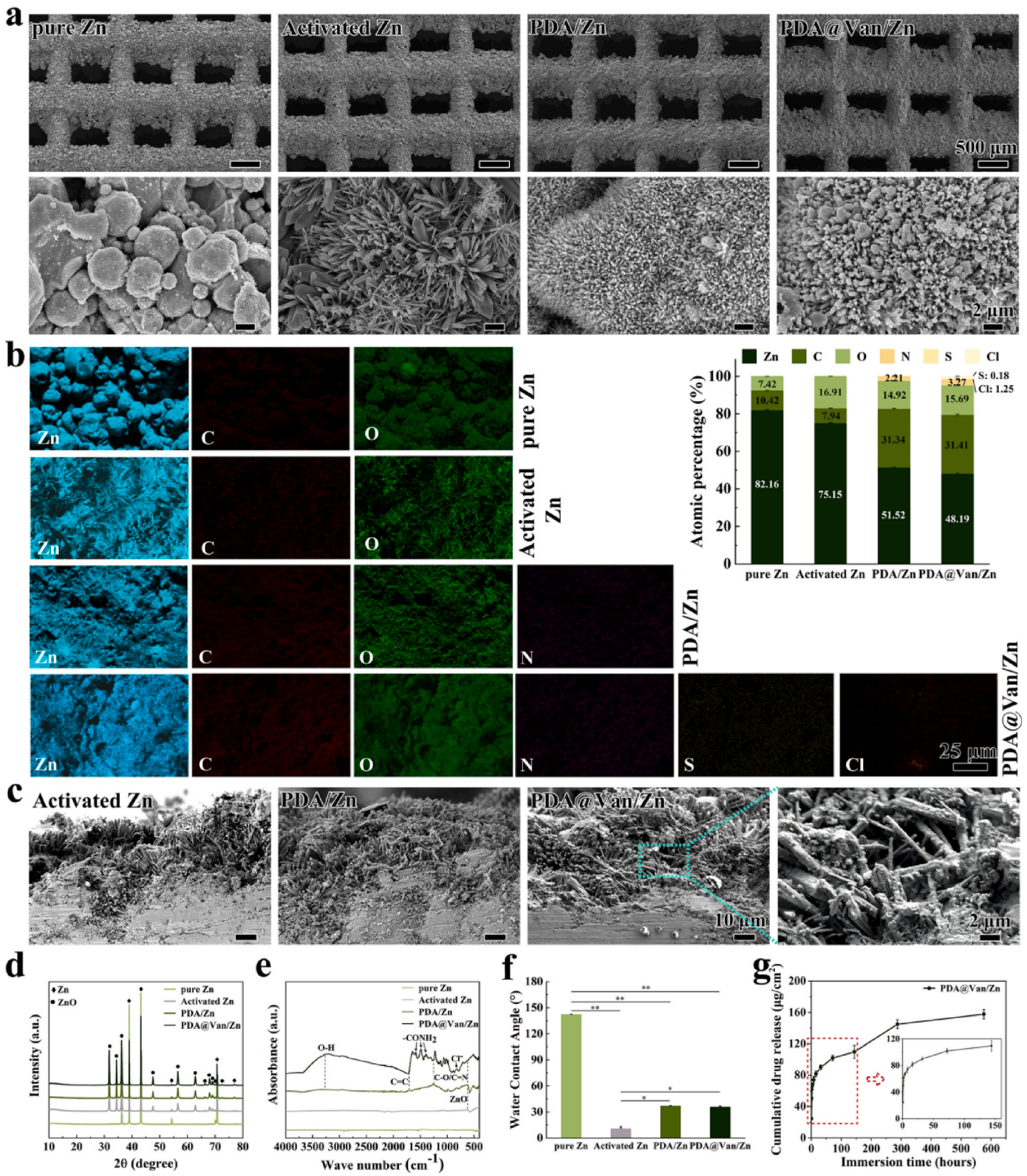

Fig. 1. (a) SEM observation and (b) EDS analysis of pure Zn, PDA/Zn and PDA@Van/Zn scaffolds; (c) Cross-section of coatings; (d) XRD pattern; (e)FTIR spectra; (f) Water contact angle; (g) Drug release curve of Van.

values of the PDA/Zn and PDA@Van/Zn increased to −1.297 V_{SCE} and −1.296 V_{SCE}, respectively. Meanwhile, the i_{corr} values of PDA/Zn and PDA@Van/Zn were significantly decreased compared to the pure Zn. The PDA coating efficiently improved the corrosion resistance of pure Zn as demonstrated by higher E_{corr} and lower i_{corr}. EIS measurements were presented in Fig. S2a. The radius of semicircles in the PDA/Zn and PDA@Van/Zn groups was larger than that in pure Zn group, indicating the increased corrosion resistance of coated samples. Fig. S3b showed the equivalent circuit model for the fitting of EIS. The fitting results of EIS were listed in Table S4. *Rs* represented the resistance of *m*-SBF

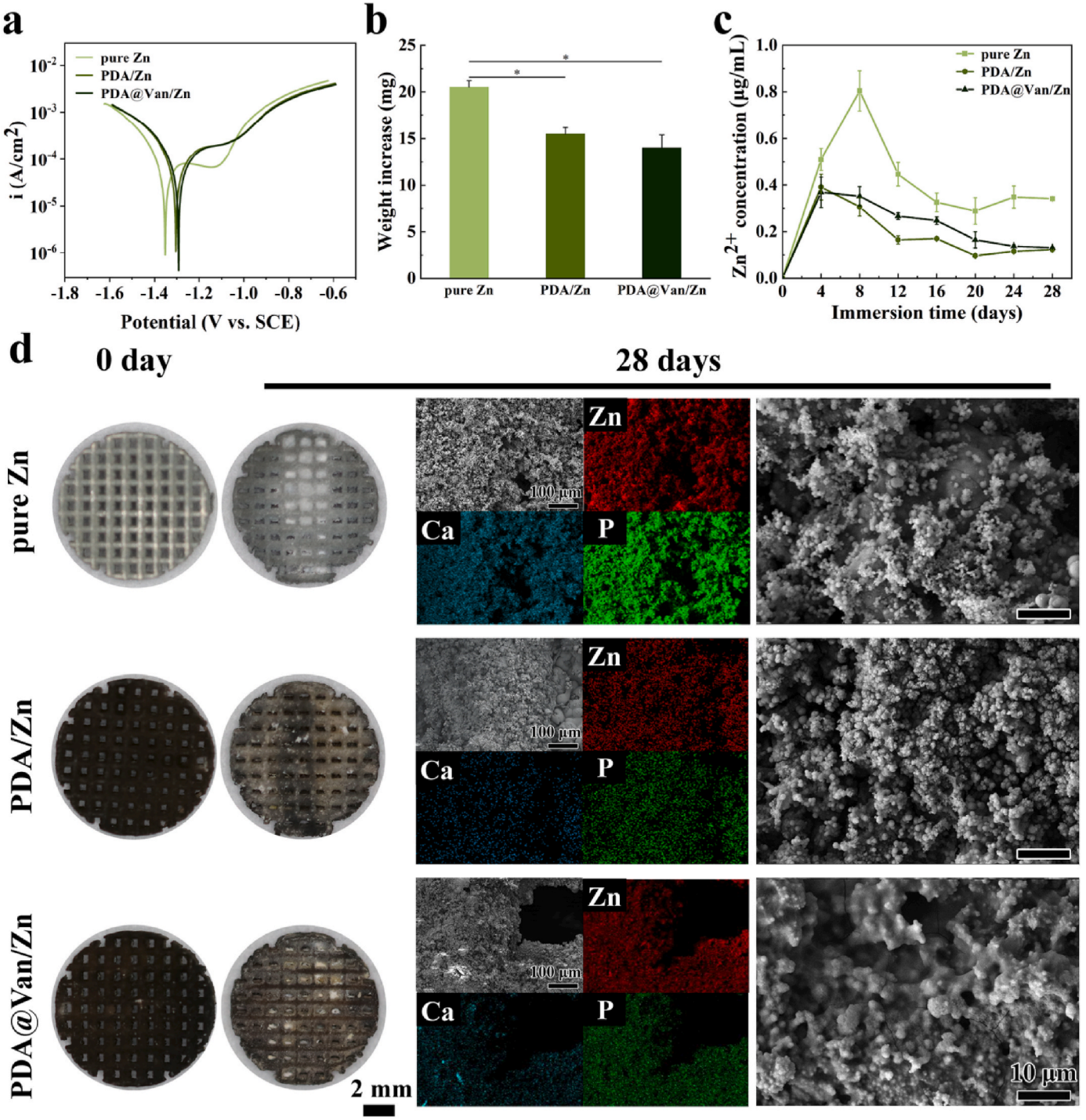

Fig. 2. *In vitro* degradation behavior: (a) PDP curves; (b) Weight increase after degradation; (c) Zn^{2+} concentration in *m*-SBF; (d) Observations of samples before and after immersion in *m*-SBF and SEM images and elemental composition analysis after immersion.

solution. R_1 and CPE_1 referred to the charge transfer resistance and double-layer capacity. The R_1 value of pure Zn, PDA/Zn and PDA@Van/Zn samples was 9.1, 46.85 and 54.71 Ω, proving the significantly enhanced corrosion resistance resulted from coating.

The immersion test was used to further analyze the long-term degradation behavior of the samples. As shown in Fig. 2d, more white degradation products were seen in the pure Zn sample. The weight change of the samples before and after immersion (Fig. 2b) also indicated fewer degradation products formed on coated Zn scaffolds. Moreover, the uniform flocculent degradation products were seen on the sample surface, and the degradation products were mainly composed of the Zn, Ca, and P elements (Fig. 2d). Fig. 2c demonstrated the variation in the concentration of Zn^{2+} released from the samples during the immersion of 28 days. The pure Zn samples released Zn^{2+} rapidly during the first 8 days, followed by a gradually decreased concentration of released Zn^{2+}. This could be attributed to the higher degradation rate of the pure Zn group, at the early stage. With the accumulation of degradation products, the degradation of the scaffolds was inhibited, and the release of Zn^{2+} was decreased gradually. Lower Zn^{2+} release concentration was observed in the coated Zn scaffolds. The release of Zn^{2+} and the accumulation of degradation products were directly correlated with the degradation rate of Zn scaffolds. The PDA coating significantly

decreased the degradation rate of pure Zn scaffolds as evidenced by the fewer degradation products and Zn^{2+} release.

3.3. In vitro tests

3.3.1. Cell viability and morphological analysis

The CCK-8 test was used to assess the cytocompatibility. The cell viability of the pure Zn group was significantly lower after 1 day of co-culture and improved after 3 and 5 days (Fig. 3b and c). For the PDA/Zn and PDA@Van/Zn groups, the cell viability was substantially higher compared to the pure Zn group. On day 5, the cell viability of the coated Zn scaffolds was approximately 120 %. This result may be related to the Zn^{2+} concentration in the sample extracts. As shown in Fig. 3a, the Zn^{2+} concentration of the pure Zn extracts was considerably higher than that of the coated scaffolds. Moreover, the addition of Van did not affect the cell viability of the coated Zn scaffolds. The result of live/dead cell staining was shown in Fig. 3d. The pure Zn group exhibited a fewer number of live cells and poor cell morphology. In contrast, the cells co-cultured with coated Zn scaffold extracts demonstrated an increased cell number and better cell morphology. According to Fig. 3e, fewer cells were found on the surface of the pure Zn scaffolds, compared to the other two groups. Moreover, the cells were not significantly stretched and spherical in shape. For PDA/Zn and PDA@Van/Zn groups, more number and better stretching morphology of cells were observed on the surface of the scaffolds.

3.3.2. In vitro osteogenic differentiation

ALP staining and activity analysis were used to assess the early osteogenic differentiation of MC3T3-E1 cells. The PDA/Zn and PDA@-Van/Zn groups exhibited higher significant ALP activity (Fig. 4a). The quantitative results of ALP activity also confirmed the higher ALP expression in the coated Zn scaffolds (Fig. 4c and d). The formation of mineralized nodules was a late-stage marker of osteogenic differentiation. The number of mineralized nodules in the coated Zn groups was significantly more than that of the pure Zn scaffold group (Fig. 4b, e). This indicated that the PDA coating could improve the ability of pure Zn scaffolds to induce osteogenic differentiation.

The relative expression levels of osteogenesis-related genes were used to further assess the osteogenic differentiation capacity of the samples. The results evidenced that the gene expression levels of Runx-2, OCN, and OPN genes were substantially higher in PDA/Zn and PDA@Van/Zn compared to pure Zn (Fig. 4f ~ h). This further indicated that PDA coating enhanced the ability of pure Zn scaffolds to induce osteogenic differentiation.

3.3.3. In vitro antibacterial activity

The adhesion morphology of *S. aureus* and *E. coli* was shown in Fig. 5a and b. There were many *S. aureuss* on the surface of pure Zn and PDA/Zn, and the number of live bacteria on the PDA/Zn was lower compared to pure Zn. However, *S. aureus* was barely visible on the surface of PDA@Van/Zn, and the morphology was severely distorted. The SEM images of *E. coli* showed similar results to *S. aureus*. According to Fig. 5c and d, the number of *S. aureus* and *E. coli* in each group was considerably lower than that in the negative control group, in the order of pure Zn, PDA/Zn, and PDA@Van/Zn. This indicated that all samples exhibit an antibacterial effect on both bacteria, with PDA@Van/Zn displaying the most pronounced antibacterial effect. As shown in Fig. 5e, the results showed that the PDA@Van/Zn scaffolds had strong antibacterial ability, after 3 and 7 days of antibacterial drugs release in PBS solution, which could be attributed to the long-lasting release of Van in the PDA coating. However, the pure Zn and PDA/Zn groups exhibited weaker antibacterial ability than PDA@Van/Zn, and further weakened with time. This could be explained as a result of the generation of biodegradation products on the surface of the scaffolds, which inhibited the release of Zn^{2+}.

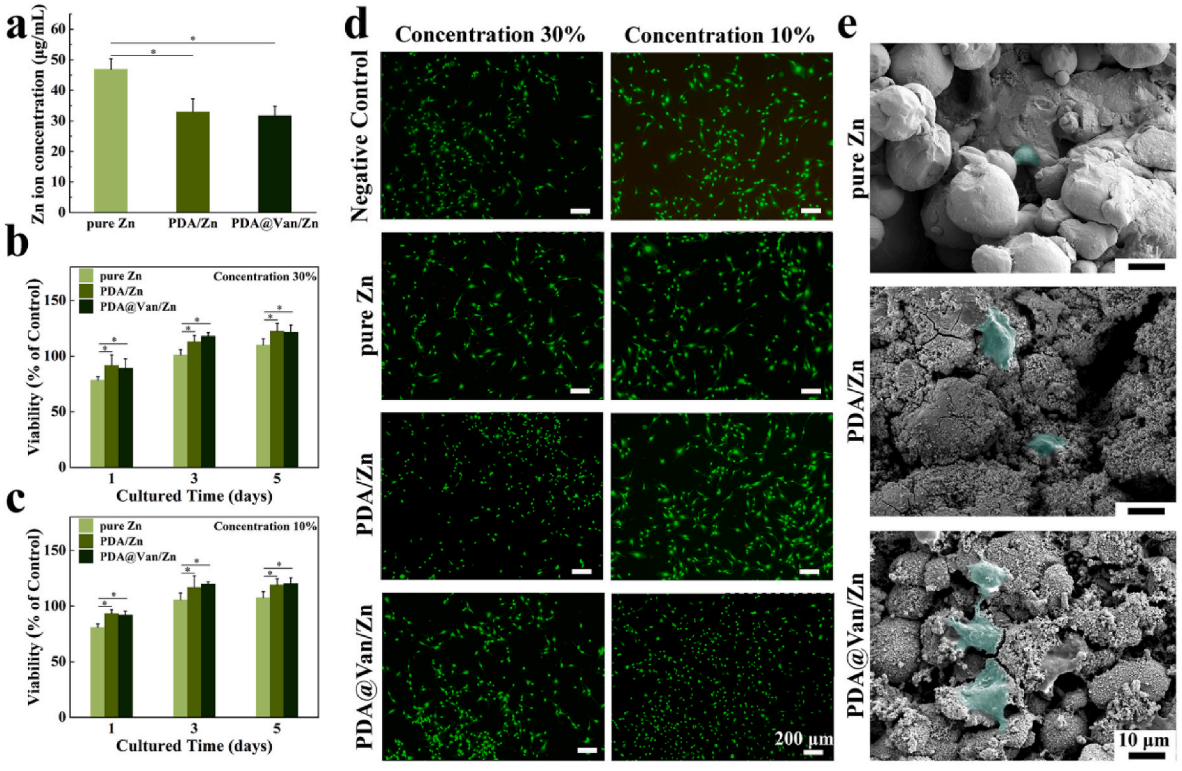

Fig. 3. *In vitro* cytocompatibility: (a) Zn^{2+} concentration in extracts; (b, c) cell viability of MC3T3-E1 co-cultured with different sample extracts; (d) Live/Dead staining images of MC3T3-E1 cells; (e) MC3T3-E1 cells' morphology on the surface of samples after co-culture.

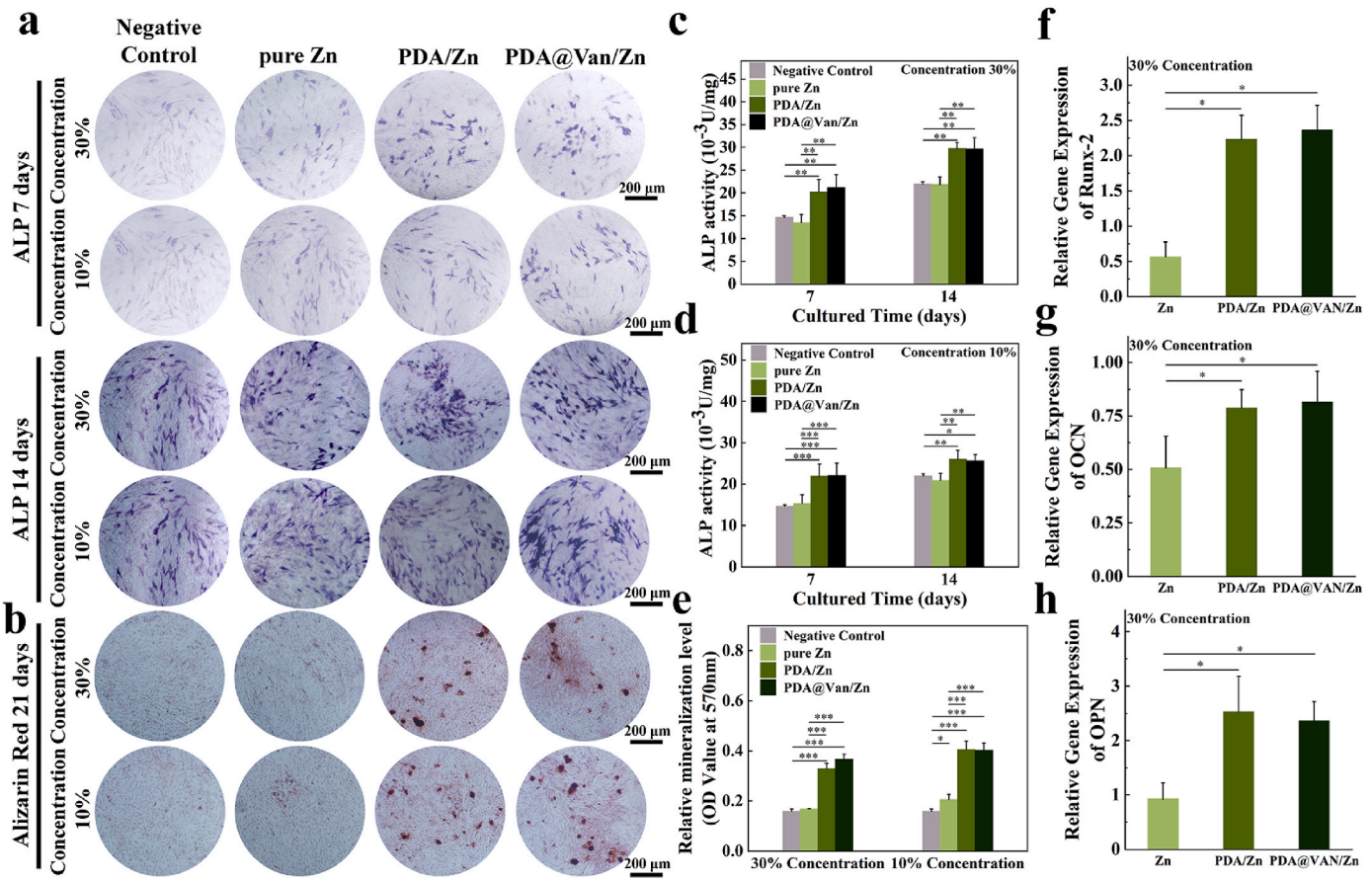

Fig. 4. *In vitro* osteogenic differentiation: (a) ALP staining; (b) Alizarin Red staining; (c, d) ALP activity of MC3T3-E1 cells co-cultured with different sample extracts for 7 and 14 days; (e) Semi-quantitative analysis of mineralization levels; (f ~ h) The expression of RUNX-2, OCN, and OPN genes of MC3T3-E1 cells co-cultured with different samples extracts for 7 days.

3.4. *In vivo tests*

3.4.1. *Micro-CT*

The Micro-CT of rat femoral condyles obtained at week 4, 8, and 12 after implantation were shown in Fig. 6a. The amount of new bone (depicted in orange) grew steadily over time, and the amount of new bone around the PDA/Zn and PDA@Van/Zn coatings were considerably greater than the pure Zn. Four Micro-CT indicators, including BV/TV, Th.N, Th.Tb and Th. Sp, were used to further quantitatively analyze the bone defect repair ability of the scaffolds (Fig. 6b ~ e). Higher BV/TV, Th.N, and Th.Tb were observed in coated scaffolds. The Th. Sp of coated scaffolds was lower than the pure Zn. These results indicated that PDA/Zn and PDA@Van/Zn scaffolds had superior osteogenic ability.

3.4.2. *Histological analysis*

The results of the histological analysis were shown in Fig. 7, where the red area represented new bone. The amount of new bone in each group grew gradually over time, with PDA/Zn and PDA@Van/Zn groups exhibiting more new bone formation compared to pure Zn. A fibrous tissue layer was observed between pure Zn and new bone. In contrast, PDA/Zn and PDA@Van/Zn demonstrated a tight connection to the newborn bone, and showed substantial inward bone growth, indicating the superior osseointegration ability. These results were in line with the results of Micro-CT, suggesting that both PDA and PDA@Van coating promoted the osteogenic activity of the pure Zn *in vivo*.

H&E staining sections of the vital organs, including the heart, liver, spleen, lungs, and kidneys, were prepared to evaluate the biosafety of the scaffolds *in vivo*. The results indicated that no histological abnormalities were observed in the sections, suggesting that all scaffolds exhibited favorable biosafety *in vivo* (Fig. S4).

3.4.3. *In vivo antibacterial activity*

The femur specimens with scaffolds from infected bone defects were used to evaluate the antibacterial activity. In pure Zn group, a substantial number of colonies were found on the surface of implants and bone tissue, while PDA/Zn had fewer bacteria compared to pure Zn, and only scattered bacteria were observed in PDA@Van/Zn (Fig. 8a). The bacteria on the scaffolds and bone tissue surfaces followed the order: pure Zn > PDA/Zn > PDA@Van/Zn (Fig. 8b). The H&E staining specimens of the decalcified bone were shown in Fig. 8c. Pure Zn group showed obvious inflammatory corpuscle infiltrates, abscess formation, and bone destruction. PDA/Zn group displayed a reduced presence of infiltrating inflammatory corpuscle compared to pure Zn, but the infection was still existent. The PDA@Van/Zn group showed significantly fewer signs of infection, with only a few inflammatory corpuscle infiltrates.

4. Discussion

4.1. *Preparation of PDA@Van coating*

Pure Zn scaffolds fabricated by L-PBF have exhibited significant potential in orthopedic applications owing to their osteogenic and antibacterial properties [54,55]. The biocompatibility and osteogenic ability at the early stage are highly related to the concentration of Zn^{2+} release. The interconnected porous structures amplify the surface area exposed to the corrosive environment, resulting in substantial Zn^{2+} release. The substantial release of Zn^{2+} during the initial degradation of

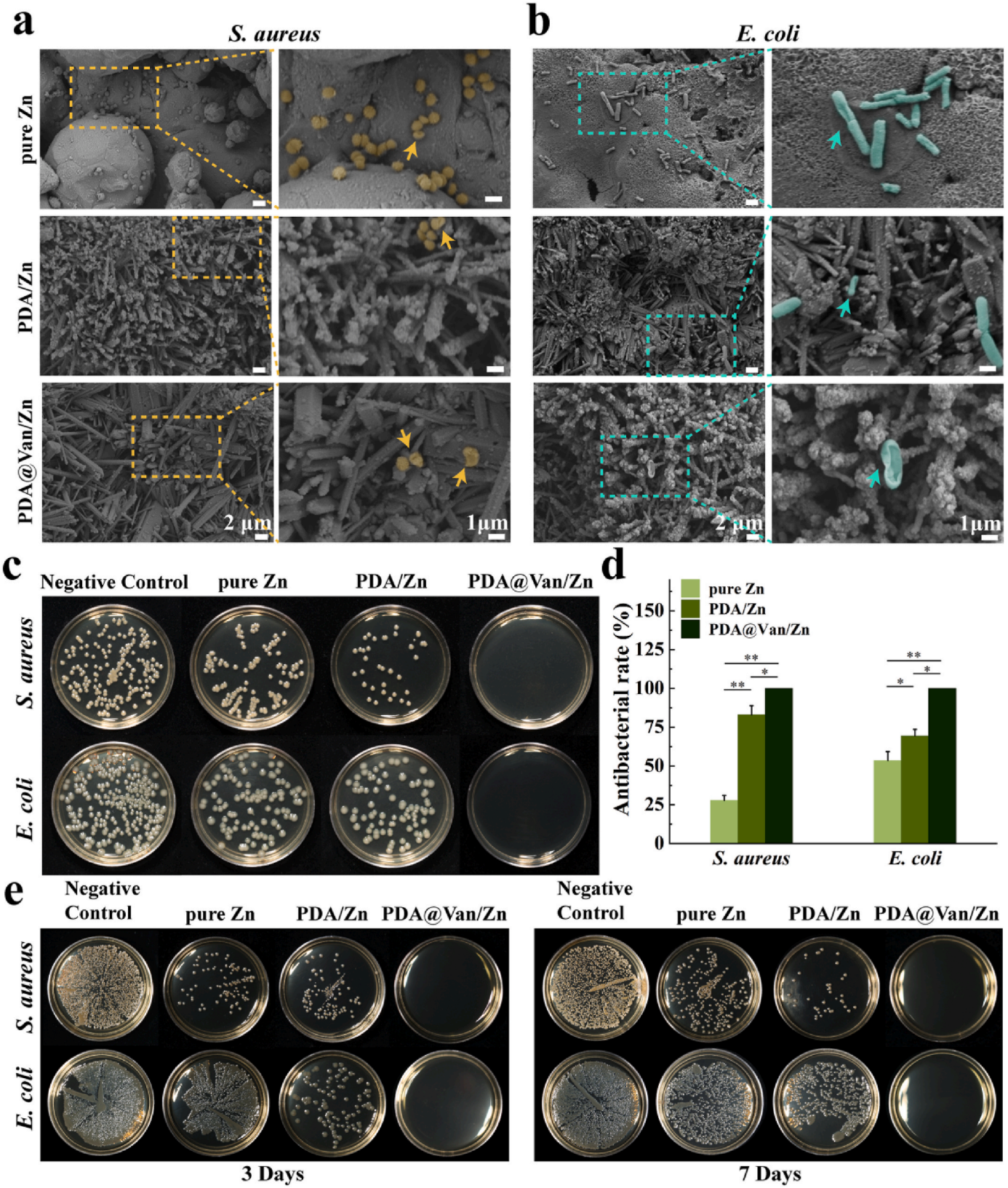

Fig. 5. *In vitro* antibacterial activity: Bacterial morphology on the surface of samples after co-culture with (a) *S. aureus* and (b) *E. coli* (arrows tips indicated dead bacteria with broken and incomplete bacterial cell walls); (c) Images of *S. aureus* and *E. coli* on TSA after co-cultured with samples; (d) Antibacterial rates calculated by colony counting method; (e) Antibacterial abilities of the samples after incubation with PBS for 3, 7 days.

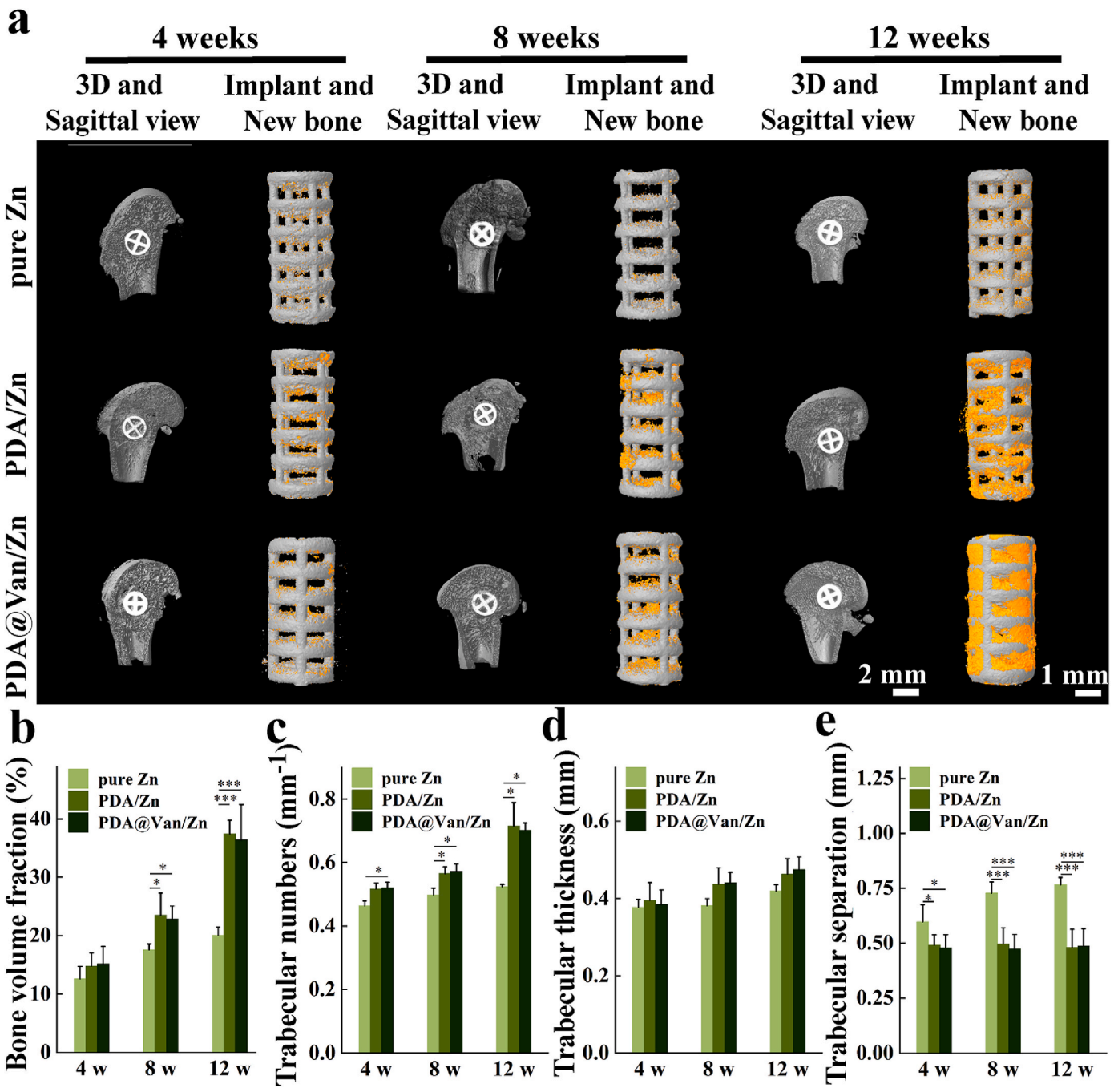

Fig. 6. *In vivo* osteogenic ability: (a) Micro-CT reconstructions of the bone defect repair in the pure Zn, PDA/Zn, and PDA@Van/Zn groups; (b ~ e) Quantification of osteogenic ability: BV/TV, Th.N, Th.Tb, Th. Sp.

pure Zn can result in detrimental effects [5]. Decreasing the degradation rate of the scaffolds is effective in keeping a low concentration of Zn^{2+} in local tissues for promoting bone repair. However, the low Zn^{2+} concentrations are adverse to the antibacterial properties of the scaffolds. For these reasons, a homogeneous and stable PDA coating was constructed on the surface of pure Zn porous scaffolds in this study. This coating aimed to retard scaffold degradation, improve biocompatibility, and promote osteogenic activity. Additionally, antibacterial drugs loaded by the PDA coating could also enhance the antibacterial abilities of the scaffolds [33].

The characteristics and structures of pure Zn porous scaffolds by L-PBF are not conducive to the fabrication of surface coatings. Firstly, the hydrophobic surface of pure Zn (Fig. 1f) is not favorable to coating adherence. Secondly, the pure Zn will slightly degrade in the coating deposition solution, disturbing the coating-to-substrate adhesion. Finally, pure Zn porous scaffolds have a complicated inner surface structure, which leads to significant difficulty in depositing uniform coatings. To overcome the above problems, we prepared a uniform ZnO crystal layer on the surface of Zn scaffolds by alkali-heat treatment, which greatly improved the surface wettability (Fig. 1f), thus beneficial to the adhesion of the PDA coating. This special crystal layer also provided stable binding sites for the adhesion of PDA (Fig. 1a).

Factors such as DA concentration, solvent, pH, and temperature all influence the quality of PDA coatings. Reportedly, a suitable concentration of DA, which was dissolved in a mixed ethanol/water solution with a volume fraction of 25 %–40 % and a pH value adjusted to weak

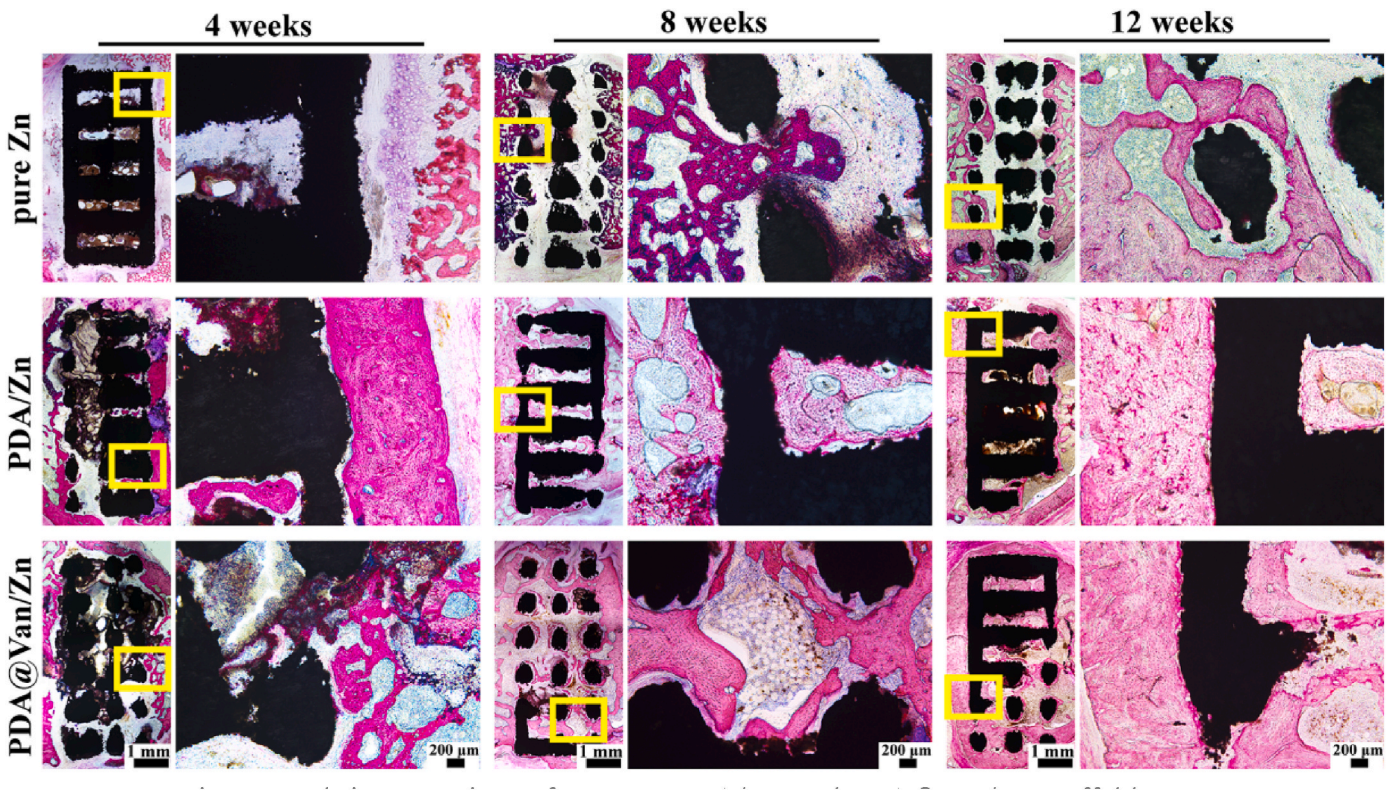

Fig. 7. Hard-tissue sections of pure Zn, PDA/Zn, and PDA@Van/Zn scaffolds.

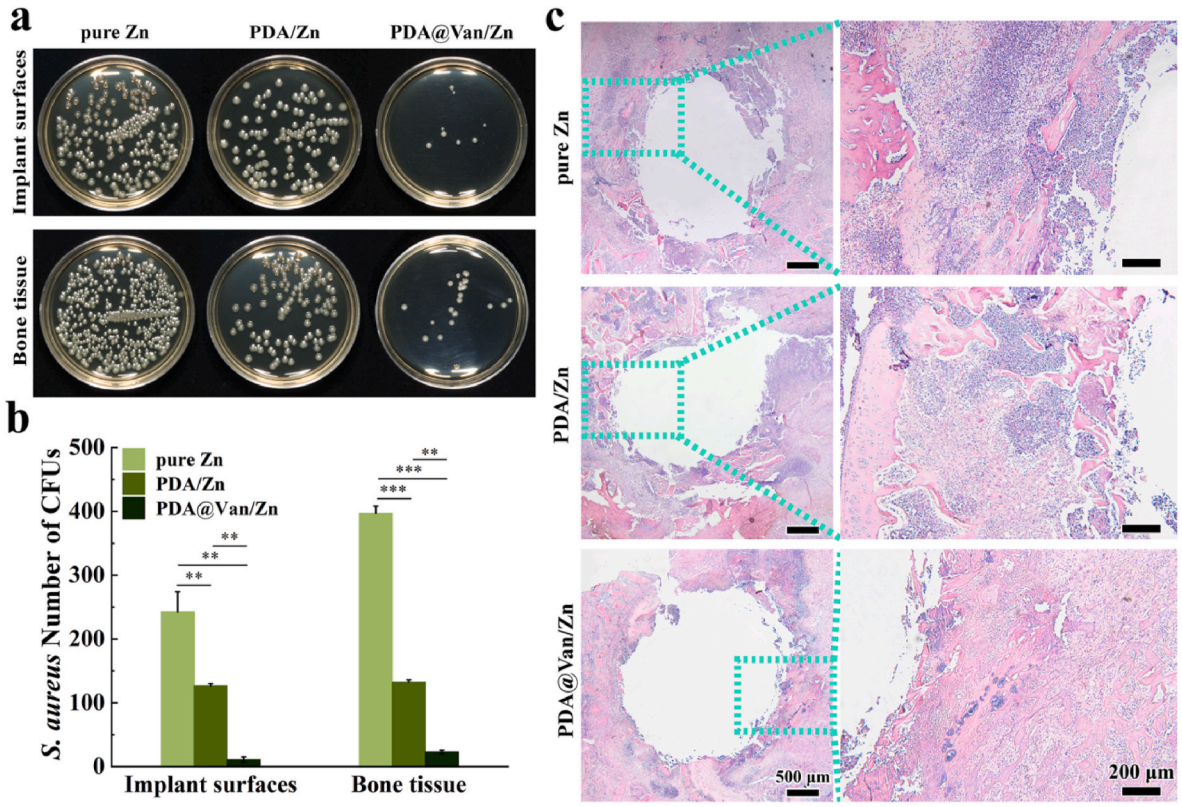

Fig. 8. *In vivo* antibacterial activity: (a) Representative images and (b) number of bacterial colonies of bacterial cultures obtained in the peri-implanted bone tissues and on the surface of implants; (c) H&E staining of the infected femoral condyle.

alkalinity using an organic base, resulted in sustained oxidation of DA as well as the formation of well-dispersed and uniformly sized PDA microspheres [52,53,56]. Pure Zn exhibited enhanced stability in solutions with pH values between 9 and 11, and did not dissolve easily. For this purpose, an ethanol/water mixture was chosen as the solvent for the PDA deposition solution and the pH value was modified by 2-piperidine ethanol to 10.5. A uniform PDA coating was successfully constructed on the surface of the pretreated scaffolds. Furthermore, the antibacterial drug Van was mixed into the PDA coating deposition solution. The PDA coating loaded with antibacterial drugs was accomplished [57]. The successful preparation of the Van-loaded PDA coating was confirmed by the alteration of the surface physicochemical characteristics of the scaffolds (Fig. 1a ~ e).

4.2. Biodegradation behavior, biocompatibility, and osteogenic activity

Zn degrades primarily through anodization to Zn^{2+} and cathodic reduction of oxygen. The degradation process at first produces ZnO and $Zn(OH)_2$ [58]. Zn^{2+} interacts with Cl^- in the medium and results in the formation of soluble chloride salts [59]. In the present study, the composition of degradation products of the scaffolds after 28 days of immersion was primarily Zn, Ca, and P. The degradation products of Zn scaffolds were generally ZnO, $Zn_5(CO_3)_2{\cdot}(OH)_6$, $Ca_3(PO_4)_2$, and $Zn_5(OH)_6Cl_6{\cdot}H_2O$ [59]. The degradation products impact the biological behavior of the cells surrounding the implant as well as the host reaction at the implant site. It had been demonstrated that local high concentrations of Zn^{2+} exhibited cytotoxicity and led to deleterious effects on bone metabolism. Controlling the release of Zn^{2+} of pure Zn scaffolds is thus an effective way to improve osteogenic activity. Yuan et al. [60] deposit a ZrO_2 blocking layer on the surface of Zn–Li alloys through the atomic layer deposition. This layer reduced Zn^{2+} release by inhibiting biodegradation. The PDA coating with Van showed a similar physical blocking effect. The coating structures prevented direct contact of corrosive media with the pure Zn substrate and considerably reduced the degradation (Fig. 2). PDA microspheres gradually diminished with degradation, and the dense structures of the coating were destroyed. The corrosive medium gradually eroded the substrate through the fine interstices between the coatings. With the development of degradation, the PDA coating may exfoliate, dissolve, and lose its degradation inhibitory effect on the substrate, resulting in increased scaffold degradation. Hence, PDA coating inhibited the rapid release of Zn^{2+} at the early stage of implantation (Fig. 2c) and considerably enhanced the biocompatibility and osteogenic activity of pure Zn scaffolds.

Zn^{2+} has been shown to have a biphasic effect on osteoprogenitor cells [61–63]. Lower concentrations of Zn^{2+} promote cell survival, proliferation, and osteogenesis, while higher concentrations lead to the opposite results. After 1 day of co-culture, the cytocompatibility of the pure Zn group was found to be less than 100 % (Fig. 3b and c). The decrease in cytocompatibility was attributed to the high concentration of released Zn^{2+}, which induced cell injury by interfering with electron transport in uncoupled mitochondria, leading to a reversible reduction in cell proliferation [63]. This reversible cell injury might be reversed as the cell grows [63], which explained the improvement in cytocompatibility after 3 and 5 days of co-culture in the pure Zn group (Fig. 3b and c). PDA-coated scaffolds demonstrated good cytocompatibility attributed to the physical blocking effect of the PDA coating, which resulted in the low concentration of Zn^{2+} release (Fig. 3a). On the other hand, the cell growth on the surface of Zn scaffolds with PDA coating was significantly better than pure Zn scaffolds, due to the good biocompatibility and hydrophilicity of PDA (Fig. 3e). Furthermore, the low concentration of Zn^{2+} in the bone environment promotes protein synthesis by activating tRNA synthases and stimulating gene expression, which increases DNA quantity in the cells, in turn promoting osteoblast differentiation and mineralization [64]. The osteogenic ability of PDA-coated scaffolds was greatly increased when compared to pure Zn scaffolds (Fig. 4), indicating that PDA coating led to the release of low concentrations of Zn^{2+} and was beneficial to cell osteogenic differentiation. Furthermore, the good biocompatibility of PDA also played a role in improving osteogenic activity. The freestanding PDA coating, without the addition of other chemical components, has been proven to enhance cell adhesion, proliferation, and osteogenic differentiation [65–67].

At 4, 8, and 12 weeks after implantation *in vivo*, superior osseointegration and bone regeneration were found in the PDA and PDA@Van-coated groups compared to the pure Zn group (Figs. 6 and 7). In the initial stage of bone defect repair, an inflammatory response and local accumulation of body fluids happened, due to edema and hematoma, accelerating the degradation rate of the Zn scaffolds [68]. The consequent excessive release of degradation products led to an unfavorable host response [69,70]. Coating with PDA and PDA@Van significantly reduced the local concentration of Zn^{2+} released from scaffolds. Meanwhile, the catechol groups in PDA had a strong chelating effect on Ca^{2+}, thus the PDA coating promoted the enrichment of Ca^{2+} on the surface of implants and provided nucleation sites for the formation of the bone apatite [71,72]. Furthermore, the wettability of the implant surface is an important factor that regulates cell adhesion, platelet activation, and tissue growth [37]. The hydrophilic groups in PDA coating improved the surface wettability of the pure Zn (Fig. 3c), enhancing osteoblast adhesion, proliferation, and mineralization. In conclusion, the improved biocompatibility and osteogenic activity of the PDA-coated Zn scaffolds are attributed to the combined effect of the slow release of Zn^{2+} and altered osteogenic-friendly physicochemical properties.

4.3. Antibacterial property

Bacterial infections have been identified as one of the global major health challenges, especially for orthopedic surgery [73]. Persistent bacteria may cause such infections during the whole surgery adhesion to biomaterials and the formation of biofilm [74,75]. A variety of bacteria, for instance, *S. aureus* and *E. coli*, have been linked to osteomyelitis, peri-implantitis, and bone-implant infections [74,75]. Biodegradable antibacterial implants can gradually disappear with degradation, depriving bacteria of a survival platform, while also maintaining anti-infection during bone repair by releasing antibacterial substances, demonstrating unique benefits in the development and design of bone implants.

The antibacterial activity of pure Zn is mostly based on released Zn^{2+}, and the Zn scaffolds can exert sustained antibacterial due to the continual release of Zn^{2+}. The antibacterial property is primarily accomplished through the following ways. Initially, Zn^{2+} can interact with the cell membranes of bacteria, enhancing membrane permeability and ultimately leading to bacterial cell rupture or death [76,77]. Secondly, Zn^{2+} can be bactericidal by inhibiting electron transport system enzymes and interacting with DNA upon entry into bacteria, thus altering bacterial metabolism [78,79]. Moreover, Zn^{2+} can catalyze the production of ROS, such as OH^-, O_2^-, and H_2O_2, resulting in cellular oxidative stress and the death of bacteria [80]. However, the high concentration of Zn^{2+} required for antibacterial activity contrasts with the low concentration of Zn^{2+} required for osteogenesis.

The PDA coating with Van was found to be significantly bactericidal against the most prevalent pathogenic bacteria associated with bone implant infections, such as *S. aureus* and *E. coli* (Fig. 5). PDA@Van/Zn porous scaffolds could immediately and in significant quantities release Van from the PDA coating at the initial stage of implantation (Fig. 8). The PDA@Van coating resulted in the rapid achievement of high local concentration levels of the antibiotics during the initial stage of implantation and sustained slow release later on, effectively inhibiting bacterial adhesion on the surface of coating and effectively killing free bacteria around the scaffolds. The release of Van dramatically improved the antibacterial ability of scaffolds to suppress infection-induced bone resorption. Local application of Van from the coating provided a safe and effective response to postoperative infections, while avoiding the harmful side effects associated with systemic application of antibiotics

[81–83]. The Van-loaded PDA coating demonstrated good biocompatibility *in vitro* and *in vivo* tests (Fig. 3, S4). This local drug delivery not only employed a lower dose than the usual method but also extended the period of antibacterial drug release at a specific spot, minimizing unnecessary dose overruns and removing the need for regular drug delivery [83]. Furthermore, the drug loading and release rate of Van could be adjusted to meet demand by modifying the concentration of Van in the deposition solution, and the number of depositions. Interestingly, it was also observed that PDA/Zn had better antibacterial properties than pure Zn (Figs. 5 and 8). This was because the cationic functional groups in PDA had the potential to bind to negatively charged bacterial membranes, altering the membrane structures and finally leading to membrane rupture. Ultimately, the antibacterial function of PDA and the stable anchorage of Van improved the antibacterial property of pure Zn scaffolds.

5. Conclusions

In vitro and *in vivo* studies were performed on biodegradable Zn porous scaffolds with a drug-loaded coating for the treatment of infected bone defects. After alkali-heat treatment, the hydrophilic surface and deposited ZnO crystal promoted the construction of a uniform PDA@-Van coating on pure Zn porous scaffolds. The coating delayed degradation through the physical blocking effect and inhibited the cytotoxicity caused by the excessive release of Zn^{2+}. PDA@Van coating greatly improved the biocompatibility and osteogenic activity of pure Zn scaffolds, which was attributable to a combination of the decreased release of Zn^{2+} and the altered osteogenic-friendly surface characteristics. PDA and Van were capable of effectively eliminating Gram-positive and negative bacteria and considerably enhanced the antibacterial properties of pure Zn scaffolds. The PDA@Van coating decreased the degradation rate of pure Zn scaffolds, which may be too slow to match the period of bone recovery. In the future, it is necessary to further investigate and optimize the biodegradable performance by approaches such as alloying and porous design. In addition, it is worthwhile to try more multifunctional surface modification such as pro-angiogenesis or immunomodulation to produce a more favorable immunological environment for osteogenesis and angiogenesis.

Ethics approval and consent to participate

The authors declare that all animal experiments are approved by the Institutional Animal Care and Use Committee (KYLL0001089) as well as the ARRIVE Guidelines. All authors comply with all relevant ethical regulations.

CRediT authorship contribution statement

Xiang Jin: Conceptualization, Data curation, Investigation, Writing - original draft. **Dongxu Xie:** Writing - original draft. **Zhenbao Zhang:** Conceptualization, Data curation, Investigation, Writing - original draft. **Aobo Liu:** Data curation, Investigation, Writing - original draft. **Menglin Wang:** Data curation, Investigation. **Jiabao Dai:** Investigation. **Xuan Wang:** Investigation. **Huanze Deng:** Investigation. **Yijie Liang:** Data curation. **Yantao Zhao:** Resources, Supervision. **Peng Wen:** Resources, Supervision, Writing - review & editing. **Yanfeng Li:** Resources, Supervision, Writing - review & editing.

Declaration of competing interest

The authors declare that they have no known competing financial interests or personal relationships that could have appeared to influence the work reported in this paper.

Data availability

Data will be made available on request.

Acknowledgment

We would like to thank all the participants in the studies. The authors would like to thank Wentao Zhang for advice on the investigation especially. This work was funded by National Natural Science Foundation of China (52175274, 51875310, 82151312 and 82272493), Beijing Natural Science Foundation (L222110, L212066), Exploration project to improve the quality of standardized training for resident Doctors in 2022, Health Care Project in 2022 (22JSZ13), PLA General Hospital New Business Support Project (XYW-202110), the Beijing Science Nova Program (20220484155), Capital clinical diagnosis and treatment technology research and transformation application project (Z201100005520060) and Key Military Medical Projects (BLB20J001).

Appendix A. Supplementary data

Supplementary data to this article can be found online at https://doi.org/10.1016/j.mtbio.2023.100885.

References

[1] D. Wu, X. Chang, J. Tian, L. Kang, Y. Wu, J. Liu, X. Wu, Y. Huang, B. Gao, H. Wang, G. Qiu, Z. Wu, Bone mesenchymal stem cells stimulation by magnetic nanoparticles and a static magnetic field: release of exosomal miR-1260a improves osteogenesis and angiogenesis, J. Nanobiotechnol. 19 (1) (2021) 209.
[2] A Nauth, E Schemitsch, B Norris, Z Nollin, JT Watson, Critical-size bone defects: is there a consensus for diagnosis and treatment? J. Orthop. Trauma 32 (Suppl 1) (2018) S7–S11.
[3] Y Liu, R Wang, S Chen, Z Xu, Q Wang, P Yuan, Y Zhou, Y Zhang, J Chen, Heparan sulfate loaded polycaprolactone-hydroxyapatite scaffolds with 3D printing for bone defect repair, Int. J. Biol. Macromol. 148 (2020) 153–162.
[4] J Zhang, Y Jiang, Z Shang, B Zhao, M Jiao, W Liu, M Cheng, B Zhai, Y Guo, B Liu, X Shi, B Ma, Biodegradable metals for bone defect repair: A systematic review and meta-analysis based on animal studies, Bioact Mater 6 (11) (2021) 4027–4052.
[5] B Jia, Z Zhang, Y Zhuang, H Yang, Y Han, Q Wu, X Jia, Y Yin, X Qu, Y Zheng, K Dai, High-strength biodegradable zinc alloy implants with antibacterial and osteogenic properties for the treatment of MRSA-induced rat osteomyelitis, Biomaterials 287 (2022) 121663.
[6] H Lin, Y Tang, TP Lozito, N Oyster, B Wang, RS Tuan, Efficient in vivo bone formation by BMP-2 engineered human mesenchymal stem cells encapsulated in a projection stereolithographically fabricated hydrogel scaffold, Stem Cell Res Ther 10 (1) (2019) 254.
[7] JM Schierholz, J Beuth, Implant infections: a haven for opportunistic bacteria, J. Hosp. Infect. 49 (2) (2001) 87–93.
[8] E Zhang, X Zhao, J Hu, R Wang, S Fu, G Qin, Antibacterial metals and alloys for potential biomedical implants, Bioact. Mater. 6 (8) (2021) 2569–2612.
[9] X Qu, H Yang, B Jia, Z Yu, Y Zheng, K Dai, Biodegradable Zn-Cu alloys show antibacterial activity against MRSA bone infection by inhibiting pathogen adhesion and biofilm formation, Acta Biomater 117 (2020) 400–417.
[10] T Miyazaki, K Ishikawa, Y Shirosaki, C Ohtsuki, Organic-inorganic composites designed for biomedical applications, Biol. Pharm. Bull. 36 (11) (2013) 1670–1675.
[11] D Xia, Y Qin, H Guo, P Wen, H Lin, M Voshage, JH Schleifenbaum, Y Cheng, Y Zheng, Additively manufactured pure zinc porous scaffolds for critical-sized bone defects of rabbit femur, Bioact. Mater. 19 (2022) 12–23.
[12] D Xia, F Yang, Y Zheng, Y Liu, Y Zhou, Research status of biodegradable metals designed for oral and maxillofacial applications: a review, Bioact. Mater. 6 (2021) 4186–4208.
[13] J Qian, W Zhang, Y Chen, P Zeng, J Wang, C Zhou, H Zeng, H Sang, N Huang, H Zhang, G Wan, Osteogenic and angiogenic bioactive collagen entrapped calcium/zinc phosphates coating on biodegradable Zn for orthopedic implant applications, Biomater. Adv. (2022) 136.
[14] Y Qiao, W Zhang, P Tian, F Meng, H Zhu, X Jiang, X Liu, PK Chu, Stimulation of bone growth following zinc incorporation into biomaterials, Biomaterials 35 (25) (2014) 6882–6897.
[15] H Yang, X Qu, W Lin, D Chen, D Zhu, K Dai, Y Zheng, Enhanced Osseointegration of Zn-Mg Composites by Tuning the Release of Zn Ions with Sacrificial Mg-Rich Anode Design, ACS Biomater Sci Eng 5 (2) (2019) 453–467.
[16] Y Zhuang, Q Liu, G Jia, H Li, G Yuan, H Yu, A biomimetic zinc alloy scaffold coated with brushite for enhanced cranial bone regeneration, ACS Biomater. Sci. Eng. 7 (3) (2021) 893–903.
[17] H Yang, C Wang, C Liu, H Chen, Y Wu, J Han, Z Jia, W Lin, D Zhang, W Li, W Yuan, H Guo, H Li, G Yang, D Kong, D Zhu, K Takashima, L Ruan, J Nie, X Li, Y Zheng,

Evolution of the degradation mechanism of pure zinc stent in the one-year study of rabbit abdominal aorta model, Biomaterials 145 (2017) 92–105.
[18] PK Bowen, RJ Guillory 2nd, ER Shearier, JM Seitz, J Drelich, M Bocks, F Zhao, J Goldman, Metallic zinc exhibits optimal biocompatibility for bioabsorbable endovascular stents, Mater. Sci. Eng. C Mater. Biol. Appl. 56 (2015) 467–472.
[19] Y Liu, T Du, A Qiao, Y Mu, H Yang, Zinc-based biodegradable materials for orthopaedic internal fixation, J. Funct. Biomater. 13 (4) (2022) 164.
[20] Y Qin, P Wen, H Guo, D Xia, Y Zheng, L Jauer, R Poprawe, M Voshage, JH Schleifenbaum, Additive manufacturing of biodegradable metals: Current research status and future perspectives, Acta Biomater. 98 (2019) 3–22.
[21] A Liu, Y Lu, J Dai, P Wen, D Xia, Y Zheng, Mechanical properties, in vitro biodegradable behavior, biocompatibility and osteogenic ability of additively manufactured Zn-0.8Li-0.1Mg alloy scaffolds, Biomater. Adv. 153 (2023) 213571.
[22] X Gu, N Li, Y Zheng, F Kang, J Wang, L Ruan, In vitro study on equal channel angular pressing AZ31 magnesium alloy with and without back pressure, Mater. Sci. Eng. B Solid-State Mater. Adv. Technol. 176 (2011) 1802–1806.
[23] J Wieding, T Lindner, P Bergschmidt, R Bader, Biomechanical stability of novel mechanically adapted open-porous titanium scaffolds in metatarsal bone defects of sheep, Biomaterials 46 (2015) 35–47.
[24] Z Feng, J Liu, C Shen, N Lu, Y Zhang, Y Yang, F Qi, Biotin-avidin mediates the binding of adipose-derived stem cells to a porous β-tricalcium phosphate scaffold: Mandibular regeneration, Exp. Ther. Med. 11 (3) (2016) 737–746.
[25] A Liu, M Sun, X Yang, C Ma, Y Liu, X Yang, S Yan, Z Gou, Three-dimensional printing akermanite porous scaffolds for load-bearing bone defect repair: An investigation of osteogenic capability and mechanical evolution, J. Biomater. Appl. 31 (5) (2016) 650–660.
[26] E Tayton, M Purcell, JO Smith, S Lanham, SM Howdle, KM Shakesheff, A Goodship, G Blunn, D Fowler, DG Dunlop, RO Oreffo, The scale-up of a tissue engineered porous hydroxyapatite polymer composite scaffold for use in bone repair: an ovine femoral condyle defect study, J Biomed Mater Res A 103 (4) (2015) 1346–1356.
[27] P Wen, M Voshage, L Jauer, Y Chen, Y Qin, R Poprawe, J Schleifenbaum, Laser additive manufacturing of Zn metal parts for biodegradable applications: processing, formation quality and mechanical properties, Mater. Des 155 (2018) 36–45.
[28] Y Qin, H Yang, A Liu, J Dai, P Wen, Y Zheng, Y Tian, S Li, X Wang, Processing optimization, mechanical properties, corrosion behavior and cytocompatibility of additively manufactured Zn-0.7Li biodegradable metals, Acta Biomate, 142 (2022) 388–401.
[29] D Zhao, K Yu, T Sun, X Jing, Y Wan, K Chen, H Gao, Y Wang, L Chen, X Guo, Q Wei, Material–Structure–Function Integrated Additive Manufacturing of Degradable Metallic Bone Implants for Load-Bearing Applications, Adv Funct Mater (2023) 2213128.
[30] X. Qu, H. Yang, B. Jia, M. Wang, B. Yue, Y. Zheng, K. Dai, Zinc alloy-based bone internal fixation screw with antibacterial and anti-osteolytic properties, Bioact. Mater. 6 (12) (2021) 4607–4624.
[31] H. Yang, B. Jia, Z. Zhang, X. Qu, G. Li, W. Lin, D. Zhu, K. Dai, Y. Zheng, Alloying design of biodegradable zinc as promising bone implants for load-bearing applications, Nat. Commun. 11 (1) (2020) 401.
[32] J. Wu, L. Wang, J. He, C. Zhu, In vitro cytotoxicity of Cu^{2+}, Zn^{2+}, Ag^{+} and their mixtures on primary human endometrial epithelial cells, Contraception 85 (5) (2012) 509–518.
[33] S. Huang, N. Liang, Y. Hu, X. Zhou, N. Abidi, Polydopamine-Assisted surface modification for, Bone Biosubstitutes. Biomed Res Int (2016), 2389895.
[34] Y. Huang, Y.X. Zhang, M.Y. Li, H. Yang, J.Y. Liang, Y. Chen, Y.S. Zhang, X. Huang, L. Xie, H. Lin, H.X. Qiao, J.P. Lan, Physicochemical, osteogenic and antimicrobial properties of graphene oxide reinforced silver/strontium-doped hydroxyapatite on titanium for potential orthopedic applications, Surf. Coating. Technol. 446 (2022), 128788.
[35] F.H. Jia, D.Y. Xu, Y.X. Sun, W.J. Jiang, H. Yang, A.Q. Bian, Y.H. Liu, K.J. Liu, S. Zhang, Y.C. Wang, H.X. Qiao, H. Lin, J.P. Lan, Y. Huang, Strontium-calcium doped titanium dioxide nanotubes loaded with GL13K for promotion of antibacterial activity, anti-Inflammation, and vascularized bone regeneration, Ceram. Int. 49 (22) (2023) 35703–35721.
[36] Y. Su, K. Wang, J. Gao, Y. Yang, Y.X. Qin, Y. Zheng, D. Zhu, Enhanced cytocompatibility and antibacterial property of zinc phosphate coating on biodegradable zinc materials, Acta Biomater. 98 (2019) 174–185.
[37] E. Jablonská, D. Vojtěch, M. Fousová, J. Kubásek, J. Lipov, J. Fojt, T. Ruml, Influence of surface pre-treatment on the cytocompatibility of a novel biodegradable ZnMg alloy, Mater. Sci. Eng., C 68 (2016) 198–204.
[38] X. Mo, J. Qian, Y. Chen, W. Zhang, P. Xian, S. Tang, C. Zhou, N. Huang, H. Ji, E. Luo, H. Zhang, G. Wan, Corrosion and degradation decelerating alendronate embedded zinc phosphate hybrid coating on biodegradable Zn biomaterials, Corrosion Sci. 184 (2021), 109398.
[39] B. Joddar, A. Albayrak, J. Kang, M. Nishihara, H. Abe, Y. Ito, Sustained delivery of siRNA from dopamine-coated stainless steel surfaces, Acta Biomater. 9 (5) (2013) 6753–6761.
[40] Y. Zhao, X. Chen, S. Li, R. Zeng, F. Zhang, Z. Wang, S. Guan, Corrosion resistance and drug release profile of gentamicin-loaded polyelectrolyte multilayers on magnesium alloys: effects of heat treatment, J. Colloid Interface Sci. 547 (2019) 309–317.
[41] X. Ren, H.C. van der Mei, Y. Ren, H.J. Busscher, B.W. Peterson, Antimicrobial loading of nanotubular titanium surfaces favoring surface coverage by mammalian cells over bacterial colonization, Mater. Sci. Eng., C 123 (2021), 112021.
[42] W. Yuan, D. Xia, S. Wu, Y. Zheng, Z. Guan, J.V. Rau, A review on current research status of the surface modification of Zn-based biodegradable metals, Bioact. Mater. 7 (2022) 192–216.
[43] A. Fattah-alhosseini, K. Babaei, M. Molaei, Plasma electrolytic oxidation (PEO) treatment of zinc and its alloys: a review, Surface. Interfac. (2020) 18.
[44] Y.X. Shi, Z. Xue, P. Li, S. Yang, D.W. Zhang, S.X. Zhou, Z.P. Guan, Y.G. Li, L. N. Wang, Surface modification on biodegradable zinc alloys, J. Mater. Res. Technol. 25 (2023) 3670–3687.
[45] L. Su, Y. Yu, Y. Zhao, F. Liang, X. Zhang, Strong antibacterial polydopamine coatings prepared by a shaking-assisted method, Sci. Rep. 6 (2016) 1–8.
[46] B. Wang, Y. Li, S. Wang, F. Jia, A. Bian, K. Wang, L. Xie, K. Yan, H. Qiao, H. Lin, J. Lan, Y. Huang, Electrodeposited dopamine/strontium-doped hydroxyapatite composite coating on pure zinc for anti-corrosion, antimicrobial and osteogenesis, Mater. Sci. Eng., C 129 (2021), 112387.
[47] Z. Xu, T. Wang, J. Liu, Recent development of polydopamine anti-bacterial nanomaterials, Int. J. Mol. Sci. 23 (2022).
[48] G. Gao, Y. Jiang, H. Jia, F. Wu, Near-infrared light-controllable on-demand antibiotics release using thermo-sensitive hydrogel-based drug reservoir for combating bacterial infection, Biomaterials 188 (2019) 83–95.
[49] J.S. Lee, S.J. Lee, S.B. Yang, D. Lee, H. Nah, D.N. Heo, H.J. Moon, Y.S. Hwang, R. L. Reis, J.H. Moon, Facile preparation of mussel-inspired antibiotic-decorated titanium surfaces with enhanced antibacterial activity for implant applications, Appl. Surf. Sci. 496 (2019), 143675.
[50] Z. Zhang, A. Liu, J. Fan, M. Wang, J. Dai, X. Jin, H. Deng, X. Wang, Y. Liang, H. Li, Y. Zhao, P. Wen, Y. Li, A drug-loaded composite coating to improve osteogenic and antibacterial properties of Zn-1Mg porous scaffolds as biodegradable bone implants, Bioact. Mater. 27 (2023) 488–504.
[51] J. Wang, F. Witte, T. Xi, Y. Zheng, K. Yang, Y. Yang, D. Zhao, J. Meng, Y. Li, W. Li, K. Chan, L. Qin, Recommendation for modifying current cytotoxicity testing standards for biodegradable magnesium-based materials, Acta Biomater. 21 (2015) 237–249.
[52] I. You, H. Jeon, K. Lee, M. Do, Y.C. Seo, H.A. Lee, H.S. Lee, Polydopamine coating in organic solvent for material-independent immobilization of water-insoluble molecules and avoidance of substrate hydrolysis, J. Ind. Eng. Chem. 46 (2017) 379–385.
[53] X. Jiang, Y. Wang, M. Li, Selecting water-alcohol mixed solvent for synthesis of polydopamine nano-spheres using solubility parameter, Sci. Rep. 4 (2014) 15–18.
[54] Y. Zheng, X. Gu, F. Witte, Biodegradable metals, Mater. Sci. Eng. R Rep. 77 (2014) 1–34.
[55] Y. Qin, P. Wen, H. Guo, D. Xia, Y. Zheng, L. Jauer, R. Poprawe, M. Voshage, J. H. Schleifenbaum, Additive manufacturing of biodegradable metals: current research status and future perspectives, Acta Biomater. 98 (2019) 3–22.
[56] J. Yan, L. Yang, M.F. Lin, J. Ma, X. Lu, P.S. Lee, Polydopamine spheres as active templates for convenient synthesis of various nanostructures, Small 9 (2013) 596–603.
[57] Y. Fu, L. Yang, J. Zhang, J. Hu, G. Duan, X. Liu, Y. Li, Z. Gu, Polydopamine antibacterial materials, Mater. Horiz. 8 (2021) 1618–1633.
[58] Y. Liu, T. Du, A. Qiao, Y. Mu, H. Yang, Zinc-based biodegradable materials for orthopaedic internal fixation, J. Funct. Biomater. 13 (4) (2022) 164.
[59] Y. Li, P. Pavanram, J. Zhou, K. Lietaert, P. Taheri, W. Li, H. San, M. Leeflang, J. Mol, H. Jahr, A. Zadpoor, Additively manufactured biodegradable porous zinc, Acta Biomater. 101 (2020) 609–623.
[60] W. Yuan, B. Li, D. Chen, D. Zhu, Y. Han, Y. Zheng, Formation mechanism, corrosion behavior, and cytocompatibility of microarc oxidation coating on absorbable high-purity zinc, ACS Biomater. Sci. Eng. 5 (2) (2019) 487–497.
[61] J. Ma, N. Zhao, D. Zhu, Endothelial cellular responses to biodegradable metal zinc, ACS Biomater. Sci. Eng. 1 (2015) 1174–1182.
[62] J. Ma, N. Zhao, D. Zhu, Bioabsorbable zinc ion induced biphasic cellular responses in vascular smooth muscle cells, Sci. Rep. 6 (2016), 26661.
[63] T. Ma, L. Zhao, J. Zhang, R. Tang, X. Wang, N. Liu, Q. Zhang, F. Wang, M. Li, Q. Shan, Y. Yang, Q. Yin, L. Yang, Q. Gan, C. Yang, A pair of transporters controls mitochondrial Zn^{2+} levels to maintain mitochondrial homeostasis, Protein Cell 13 (3) (2022) 180–202.
[64] M. Yamaguchi, Role of nutritional zinc in the prevention of osteoporosis, Mol. Cell. Biochem. 338 (2010) 241–254.
[65] X. Liu, W. Chen, B. Shao, X. Zhang, Y. Wang, S. Zhang, W. Wu, Mussel patterned with 4D biodegrading elastomer durably recruits regenerative macrophages to promote regeneration of craniofacial bone, Biomaterials 276 (2021), 120998.
[66] H. Wang, C. Lin, X. Zhang, K. Lin, X. Wang, S.G. Shen, Mussel-inspired polydopamine coating: a general strategy to enhance osteogenic differentiation and osseointegration for diverse implants, ACS Appl. Mater. Interfaces 11 (2019) 7615–7625.
[67] W. Zhong, J. Li, C. Hu, Z. Quan, D. Jiang, G. Huang, Z. Wang, 3D-printed titanium implant-coated polydopamine for repairing femoral condyle defects in rabbits, J. Orthop. Surg. Res. 15 (1) (2020) 102.
[68] R. Marsell, T.A. Einhorn, The biology of fracture healing, Injury 42 (2011) 551–555.
[69] J. Anderson, Biological responses to materials, Annu. Rev. Mater. Res. 31 (2001) 81–110.
[70] D. Williams, On the mechanisms of biocompatibility, Biomaterials 29 (2008) 2941–2953.
[71] J. Ryu, S.H. Ku, M. Lee, C.B. Park, Bone-like peptide/hydroxyapatite nanocomposites assembled with multi-level hierarchical structures, Soft Matter 7 (2011) 7201–7206.
[72] S. Kim, C.B. Park, Mussel-inspired transformation of $CaCO_3$ to bone minerals, Biomaterials 31 (25) (2010) 6628–6634.
[73] X. He, E. Obeng, X. Sun, N. Kwon, J. Shen, J. Yoon, Polydopamine, harness of the antibacterial potentials-A review, Mater Today Bio 15 (2022), 100329.

[74] W.J. Metsemakers, M. Morgenstern, M.A. McNally, T.F. Moriarty, I. McFadyen, M. Scarborough, et al., Fracture-related infection: a consensus on definition from an international expert group, Injury 49 (2018) 505–510.
[75] P.A. Norowski Jr., J.D. Bumgardner, Biomaterial and antibiotic strategies for peri-implantitis: a review, J. Biomed. Mater. Res. B Appl. Biomater. 88 (2) (2009) 530–543.
[76] Y. Wang, A. Cao, Y. Jiang, X. Zhang, J. Liu, Y. Liu, H. Wang, Superior antibacterial activity of zinc oxide/graphene oxide composites originating from high zinc concentration localized around bacteria, ACS Appl. Mater. Interfaces 6 (4) (2014) 2791–2798.
[77] S. Silver, L.T. Phung, G. Silver, Silver as biocides in burn and wound dressings and bacterial resistance to silver compounds, J. Ind. Microbiol. Biotechnol. 33 (2006) 627–634.
[78] J.R. Sheldon, E.P. Skaar, Metals as phagocyte antimicrobial effectors, Curr. Opin. Immunol. 60 (2019) 1–9.
[79] K.S. Siddiqi, A. Ur Rahman, Husen A. Tajuddin, Properties of zinc oxide nanoparticles and their activity against microbes, Nanoscale Res. Lett. 13 (1) (2018) 141.
[80] T. Xia, M. Kovochich, J. Brant, M. Hotze, J. Sempf, T. Oberley, C. Sioutas, J.I. Yeh, M.R. Wiesner, A.E. Nel, Comparison of the abilities of ambient and manufactured nanoparticles to induce cellular toxicity according to an oxidative stress paradigm, Nano Lett. 6 (8) (2006) 1794–1807.
[81] U. Joosten, A. Joist, G. Gosheger, U. Liljenqvist, B. Brandt, C. von Eiff, Effectiveness of hydroxyapatite-vancomycin bone cement in the treatment of Staphylococcus aureus induced chronic osteomyelitis, Biomaterials 26 (25) (2005) 5251–5258.
[82] H.Y. Chiang, L.A. Herwaldt, A.E. Blevins, E. Cho, M.L. Schweizer, Effectiveness of local vancomycin powder to decrease surgical site infections: a meta-analysis, Spine J. 14 (3) (2014) 397–407.
[83] D. Aggarwal, V. Kumar, S. Sharma, Drug-loaded biomaterials for orthopedic applications: a review, J. Contr. Release 344 (2022) 113–133.